Flow of an incompressible fluid in a partially filled, rapidly rotating cylinder with a differentially rotating endcap

By M. A. SHADDAY,† R. J. RIBANDO and J. J. KAUZLARICH

Department of Mechanical and Aerospace Engineering,
Research Laboratories for the Engineering Sciences, School of Engineering and Applied Science,
University of Virginia, Charlottesville, Virginia 22901

The flow in a partially filled, strongly rotating cylinder with a differentially rotating endcap was studied both experimentally and numerically. The cylindrical container was mounted with a vertical axis of rotation, partially filled with an incompressible fluid, and rotated at a sufficiently high angular velocity that the fluid formed a film of essentially uniform thickness on the sidewall of the container. An axial circulation in this fluid film was induced by the differential rotation of one of the container endcaps. A laser-Doppler velocimeter was used to measure the axial and azimuthal velocity components. The experimental results were compared with a finite-difference model of the flow, and the agreement between the two was good. Boundary layers of thickness proportional to $E^{\frac{1}{3}}$, where $E = \nu/\Omega L^2$ is the Ekman number, are found both at the lateral wall and at the vertical free surface. The existence of an $E^{\frac{1}{3}}$ boundary layer along the free surface is due to the invariant structure of the $E^{\frac{1}{2}}$ Ekman layers on the horizontal surfaces with respect to a free surface. The radial transport in the Ekman layers of a partially filled rotating cylinder is essentially the same as that in a completely filled container. The axial transport, which in a completely filled container would have occurred in the volume now occupied by an empty core, is instead confined to a thin boundary layer along the free surface.

1. Introduction

A number of investigators have examined the axial flow in a liquid-filled, rotating cylindrical container where the flow is induced by the independent rotation of one endcap, but the effect of a free surface on the axial circulation in a partially filled cylinder has not been previously investigated. In this study, the axial circulation of a viscous incompressible fluid in a partially filled rotating cylinder is measured with a laser-Doppler velocimeter, and the experimental results are compared with those obtained using a numerical model of the flow.

When a cylindrical container is partially filled with an incompressible fluid and rotated at a sufficiently high angular velocity, the fluid forms a film of essentially uniform thickness on the sidewall of the container. The independent rotation of one endcap will induce an axial circulation superimposed on the flow condition of solid-body rotation. An Ekman boundary layer forms on the independently rotating endcap owing to the difference in angular velocity between the endcap and the

† Present address: Department of Mechanical Engineering, University of South Carolina, Columbia, South Carolina.
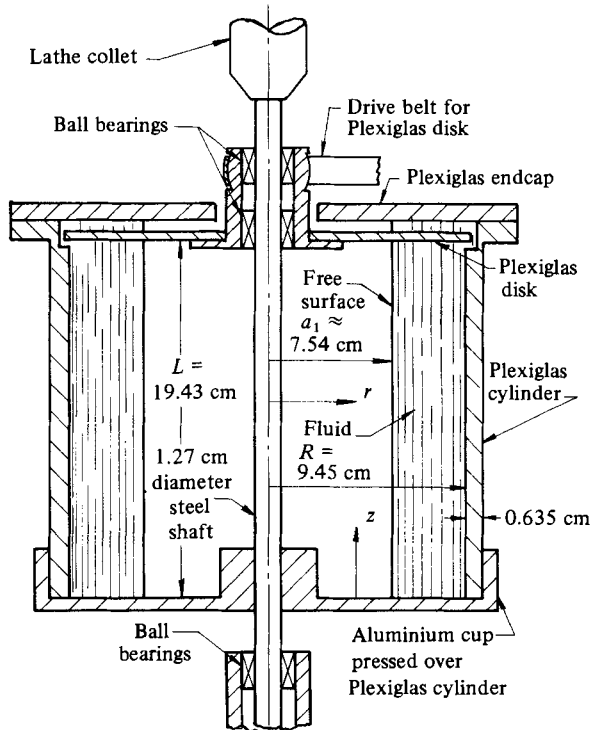
FIGURE 1. Diagram of the rotor.

cylinder, and this boundary layer acts as a centrifugal pump. In the case where the top endcap rotates faster than the cylinder, fluid is forced down the cylinder sidewall. An Ekman layer on the lower endcap serves to transport fluid radially inward towards the axis of rotation, and an axial return flow exists in the fluid interior.

There have been several studies of similar rotating flows with completely filled containers. Greenspan (1968) reviews this problem. A thin shear layer forms on the lateral wall of the cylindrical container and serves to transport fluid axially between the Ekman layers on the endcaps. The return axial flow is spread over the entire interior region. It will be shown that, in the case where the container is partially filled, a significant portion of the return axial flow is confined to a thin shear layer along the free surface.

2. Experimental apparatus and procedures

In the experimental phase of this investigation, the axial and azimuthal fluid velocity components in a partially filled rotating cylinder were measured using a laser-Doppler velocimeter (LDV). The radial profile of velocity was measured at several axial positions. A schematic diagram of the rotor assembly is shown in figure 1. The rotor is mounted on a lathe bed with its axis of rotation oriented vertically and is driven by a variable-speed motor. At 1000 r.p.m., two litres of fluid will form a film of approximately uniform thickness (1.9 cm) on the inner sidewall. Just below the top endcap is a coaxial disk, free to rotate relative to the rotor, and driven by a separate variable-speed electric motor. An axial circulation in the fluid is driven by the independent rotation of the disk.

Receiving optics
and photomultiplier
tube

Polarization
rotator

Focusing
lens

Apertures

Rotor

Fluid film

Argon-ion
laser

Polarization-
dependent
beam splitter

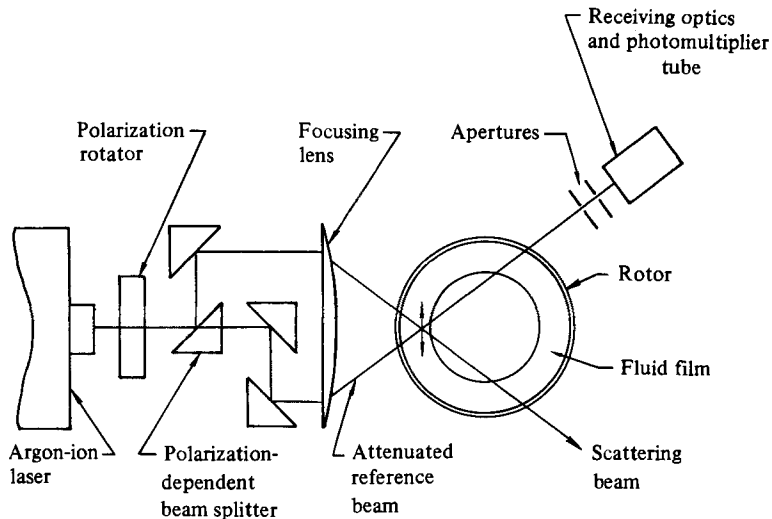Attenuated
reference
beam

Scattering
beam

FIGURE 2. Schematic diagram of the LDV system.

The fluid used in this investigation was an aqueous solution of glycerol, with a specific viscosity (the ratio of the kinematic viscosity of the solution to that of water) of 10. A specific viscosity of 10 produced axial boundary layers that were thick enough to be experimentally resolved, while insuring that the boundary layers on the rotor wall and the free surface did not overlap. The fluid was seeded with 0.5 μm polystyrene latex particles, which showed no tendency to centrifuge out of the fluid over a period of several hours.

The laser-Doppler velocimeter used was a single-component reference-beam system, using an argon-ion laser. Fluid velocities are determined from the Doppler shift of light scattered from the particles entrained in the flow. The LDV system utilized is shown schematically in figure 2. The two apertures in the receiving optics determine a solid angle of light collection, and a photomultiplier tube serves as the photodetector. The measured velocity component lies in the plane formed by the two intersecting laser beams, and is perpendicular to their bisector. The two laser beams are brought to focus at their intersection point by a 300 mm focal-length lens with a diameter of 93 mm. The beam intersection point lies along the laser-beam axis, and the transmitting optics are rotatable about this axis. The laser and transmitting optics are rigidly mounted on a common support. This support is attached to a two-degree-of-freedom traversing table capable of movement in the horizontal plane, along and perpendicular to the beam axis. The height of the LDV system is adjusted using shim blocks under the traversing table. The receiving optics are separately mounted on an adjustable support.

The photomultiplier-tube output is amplified and passed through a bandpass filter to eliminate unwanted high and low frequencies. The procedure for measuring the fluid velocity was to measure first the azimuthal velocity component. The slope of a streamline with respect to horizontal in the rotating reference frame was then measured independently. These two measurements were sufficient to calculate the axial velocity. We consider the azimuthal measurement first.

In measuring the azimuthal velocity, the Doppler frequency was determined by visual comparison of the signal on a dual-beam oscilloscope with the output of a function generator. The azimuthal velocity component in the rotating reference frame

FIGURE 3. Vector geometry of the LDV measurements.

was determined by measuring the change in Doppler frequency when the disk speed was changed from synchronous to 1050 r.p.m. (a change of $+5\%$). Then, since velocity is directly proportional to Doppler frequency, the azimuthal component in the rotating frame is given by

$$V_p = \left(\frac{f_p}{f_{sb}} - 1\right) V_{sb},$$

where the subscripts p and sb indicate perturbed and solid body respectively.

The axial velocity component cannot be directly measured with the present system because it is very small relative to the azimuthal flow. The residence time of a particle in the measurement volume formed by the intersection of the two laser beams is determined by the large azimuthal velocity, and this residence time is too short to generate a Doppler signal at the low frequency dictated by the axial velocity component. Instead the angle of a streamline in the rotating reference frame relative to the horizontal direction was determined from the relative changes in Doppler frequency of two velocity components measured in the directions $\pm 85°$ from horizontal. Figure 3 is a vector diagram of these measurements. The slope of a streamline as a function of these changes in Doppler frequency is given by (Shadday 1982)

$$\theta = \tan^{-1}\frac{a \cos 2\alpha \tan 2\alpha}{a \cos 2\alpha + b} - \alpha. \tag{1}$$

The Doppler-signal quality of the $\pm 85°$ velocity components was too poor to allow direct measurement of small frequency changes on the oscilloscope. Instead a Pulsecount frequency demodulator with a lock-and-hold circuit was used as a signal processor. The change in output of the LDV signal processor when the flow was perturbed from solid-body rotation was recorded on a plotter. A discussion of the operation of this type of signal processor is given by Durrani & Greated (1977).

The changes in Doppler frequency of the $\pm 85°$ velocity components were independently measured using the LDV system. The slope of a streamline in the rotating reference frame was determined from these measurements using (1). The axial velocity component was then determined from this angle and the previously determined azimuthal velocity component in the rotating reference frame.

The axial and azimuthal velocity distributions, as functions of radius, were measured at several axial locations by traversing the LDV optics. The radial location

of the laser-beam intersection point was determined by measuring the displacement of the LDV optics from the position where the laser beams intersected on the inner rotor wall. Appropriate corrections were made for the refraction of the laser beams by the cylindrical interfaces.

3. Numerical model

In this section the finite-difference model used in this study is described. Since the fluid velocities of interest are small deviations from the condition of solid-body rotation, it is convenient to work in a rotor-fixed reference frame. The full nonlinear axisymmetric governing equations in that frame are

$$\frac{1}{r}\frac{\partial}{\partial r}(ru) + \frac{\partial w}{\partial z} = 0, \tag{2}$$

$$\frac{\partial u}{\partial t} + \epsilon\left[\frac{1}{r}\frac{\partial}{\partial r}(ru^2) + \frac{\partial}{\partial z}(uw)\right] - \left(2 + \epsilon\frac{v}{r}\right)v = -\frac{\partial p}{\partial r} + E\left[\frac{\partial^2 u}{\partial z^2} - \frac{\partial^2 w}{\partial r\partial z}\right], \tag{3}$$

$$\frac{\partial v}{\partial t} + \epsilon\left[\frac{1}{r}\frac{\partial}{\partial r}(ruv) + \frac{\partial}{\partial z}(vw)\right] + \left(2 + \epsilon\frac{v}{r}\right)u = E\left\{\frac{\partial}{\partial r}\left[\frac{1}{r}\frac{\partial}{\partial r}(rv)\right] + \frac{\partial^2 v}{\partial z^2}\right\}, \tag{4}$$

$$\frac{\partial w}{\partial t} + \epsilon\left[\frac{1}{r}\frac{\partial}{\partial r}(ruw) + \frac{\partial}{\partial z}(w^2)\right] = -\frac{\partial p}{\partial z} + E\frac{1}{r}\frac{\partial}{\partial r}\left(r\frac{\partial w}{\partial r} - r\frac{\partial u}{\partial z}\right), \tag{5}$$

with the following non-dimensional parameters:

$$\epsilon = \frac{\Delta\Omega}{\Omega} \quad \text{(Rossby number)},$$

$$E = \frac{\nu}{\Omega L^2} \quad \text{(Ekman number)}.$$

These equations are written in the conservative or divergence form. The pressure has been combined with the centrifugal acceleration to form the reduced pressure (Greenspan 1968). Gravity has been neglected in this analysis. This assumption is justified, since the free surface of the fluid film is very nearly vertical at the angular velocities considered. At the free surface, the centrifugal acceleration is about 86 times larger than the gravitational acceleration.

The finite-difference model used to approximate the above equations uses a variable-sized mesh so that nodes may be concentrated in areas having large velocity gradients. The grid is staggered as shown in figure 4, with the velocities defined on the boundaries of the pressure control volume. The grid used had 31 points distributed axially and 20 radially. The Ekman layers on each endcap were defined by about three node points. The diffusion terms are modelled using second central differences, and upwind differencing is used on the convection terms. The momentum equations are differenced as follows:

$$\frac{u_{i,j}^{n+1} - u_{i,j}^n}{\Delta t} = (\text{convection})_{i,j}^n + 2\Omega v_{i,j}^{n+1} + \frac{1}{\rho_0}\frac{p_{i,j}^{n+1} - p_{i+1,j}^{n+1}}{\Delta r} + (\text{viscous})_{i,j}^n, \tag{6}$$

$$\frac{v_{i,j}^{n+1} - v_{i,j}^n}{\Delta t} = (\text{convection})_{i,j}^n - 2\Omega u_{i,j}^{n+1} + (\text{viscous})_{i,j}^n, \tag{7}$$

$$\frac{w_{i,j}^{n+1} - w_{i,j}^n}{\Delta t} = (\text{convection})_{i,j}^n + \frac{1}{\rho_0}\frac{p_{i,j}^{n+1} - p_{i,j+1}^{n+1}}{\Delta z} + (\text{viscous})_{i,j}^n, \tag{8}$$
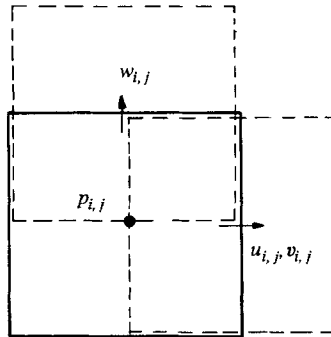
FIGURE 4. Nodal volumes used in the finite-difference simulation.

where the superscripts n and $n+1$ indicate the present and advanced time levels respectively. With the radial and azimuthal velocities defined at the same point (7) is used to eliminate $v_{i,j}^{n+1}$ in (6). This allows implicit treatment of the Coriolis terms. With explicit treatment of the Coriolis terms, there is a timestep limitation of the form $\Delta t \leqslant 1/2\Omega$ (Beardsley *et al.* 1979). Implicit treatment of these terms removes this restriction and allows use of the usual Courant criterion based on mesh size, flow velocities and fluid viscosity (Roache 1976).

No-slip boundary conditions are applied at both endcaps and the rotor sidewall. The free surface has slip boundary conditions. Small deviations from vertical are allowed at the free surface. The equations of motion are written in terms of the reduced pressure, so the restoring force due to such deviations is approximately $-\rho_0 r\Omega^2\eta$, where η is the perturbation of the vertical free surface.

The solution sequence is: substitute (6) with (7) used to eliminate $v_{i,j}^{n+1}$, and (8) and analogous expressions for $u_{i-1,j}^{n+1}$ and $w_{i,j-1}^{n+1}$ into the finite-difference approximation of the continuity equation (2) at the new time level, to form a Poisson equation for pressure at the new time level. The Poisson equation is solved using cyclic reduction (Sweet 1973) and the velocities are updated. The boundary conditions, convection and viscous terms, are then updated and the sequence is repeated until convergence is attained. For the parameters used, the characteristic spin-up time $[L^2/\Omega\nu]^{\frac{1}{2}}$ (Greenspan 1968) is about six seconds. This calculation was terminated at 7.4 s.

More details of the finite-difference algorithm may be found in Hirt (1979) and Ribando (1983). Results obtained using this finite-difference model are presented in §4 along with the experimental data.

4. Results

Velocity measurements were made at four axial positions along the rotor, and these experimental results are presented along with the predictions of the finite-difference model. In all cases the rotor angular velocity is 1000 r.p.m., and the disk at the top endcap has a velocity perturbation of $+5\%$.

Axial and azimuthal velocity profiles at four axial positions are shown in figures 5–8. For the experimental data, the dimension a_1 is the radius of the free surface determined experimentally at each axial position, and both components of velocity have been normalized by the disk peripheral velocity $U = \epsilon R\Omega$ in the rotating reference frame. The agreement between the experimental results and the finite-difference model is qualitatively good except near the free surface. This discrepancy is due in part to limitations in the radial resolution of the LDV system.
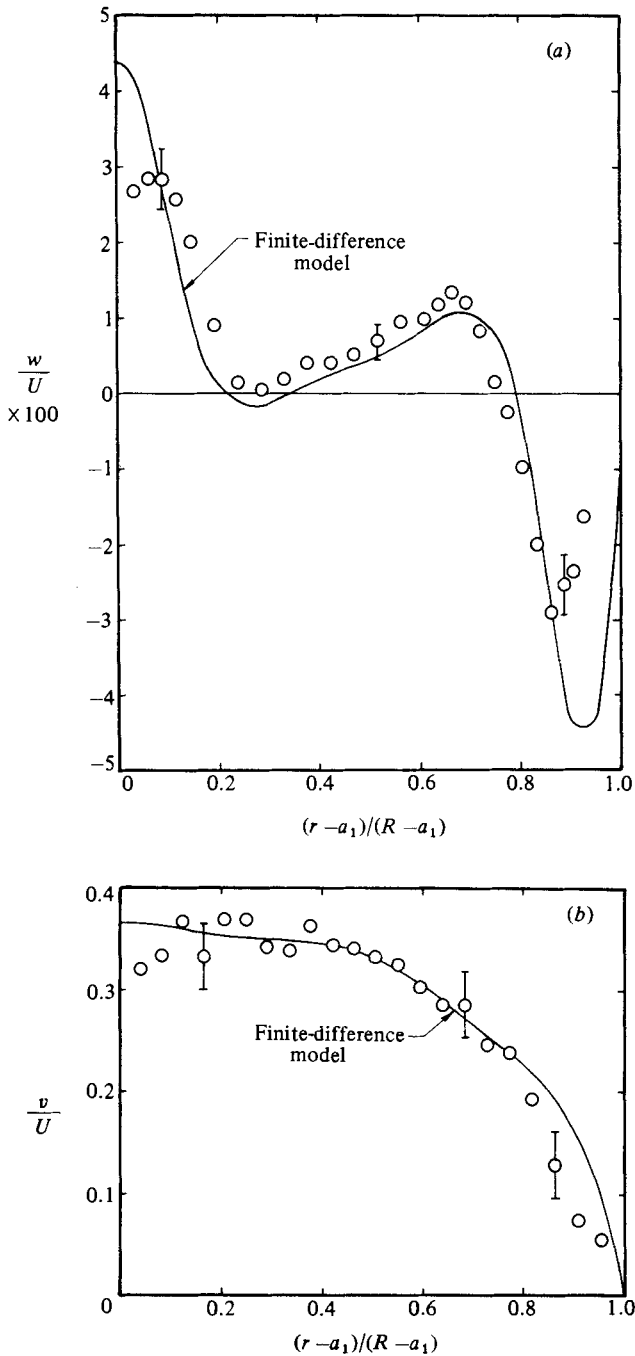
FIGURE 5. Measured and computed radial distributions of the axial (a) and azimuthal (b) velocity at $z/L = 0.83$. $E = 2.5 \times 10^{-6}$, film thickness $= 1.9$ cm, top lid overspeed $= \Delta\Omega/\Omega = 5\%$. Velocities are normalized by the disk overspeed velocity ($U = \epsilon\Omega R$); position normalized by film thickness.
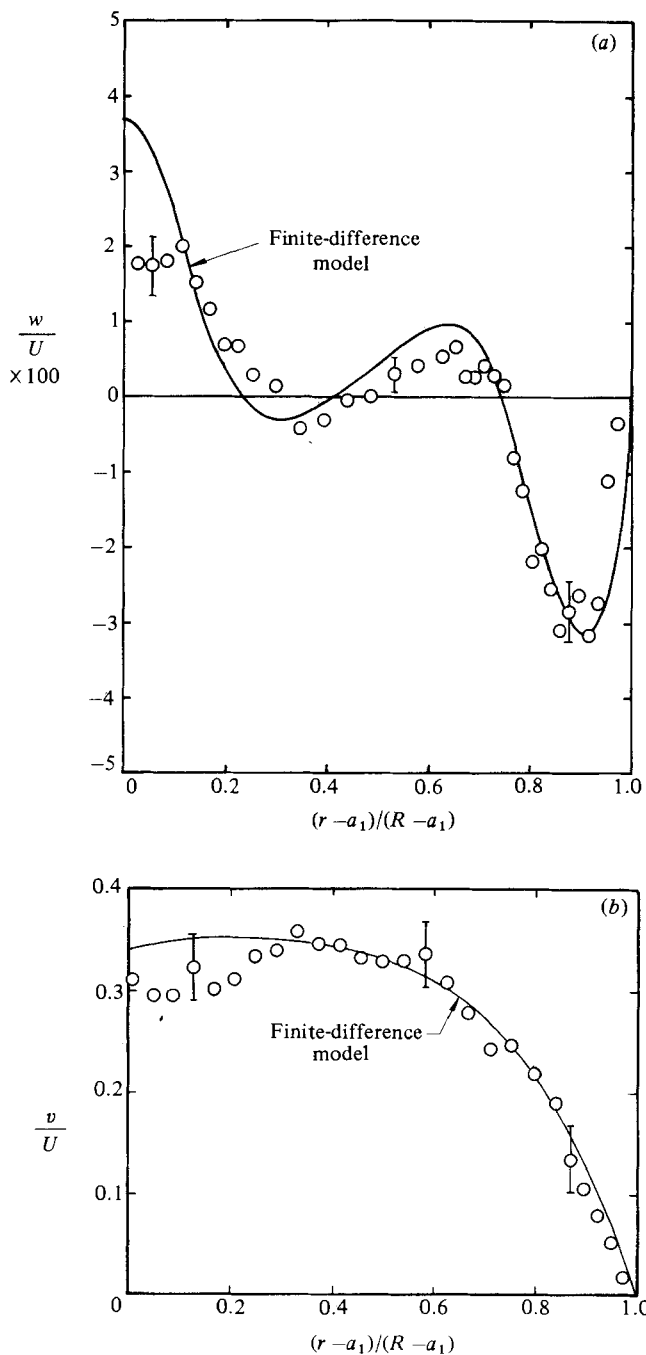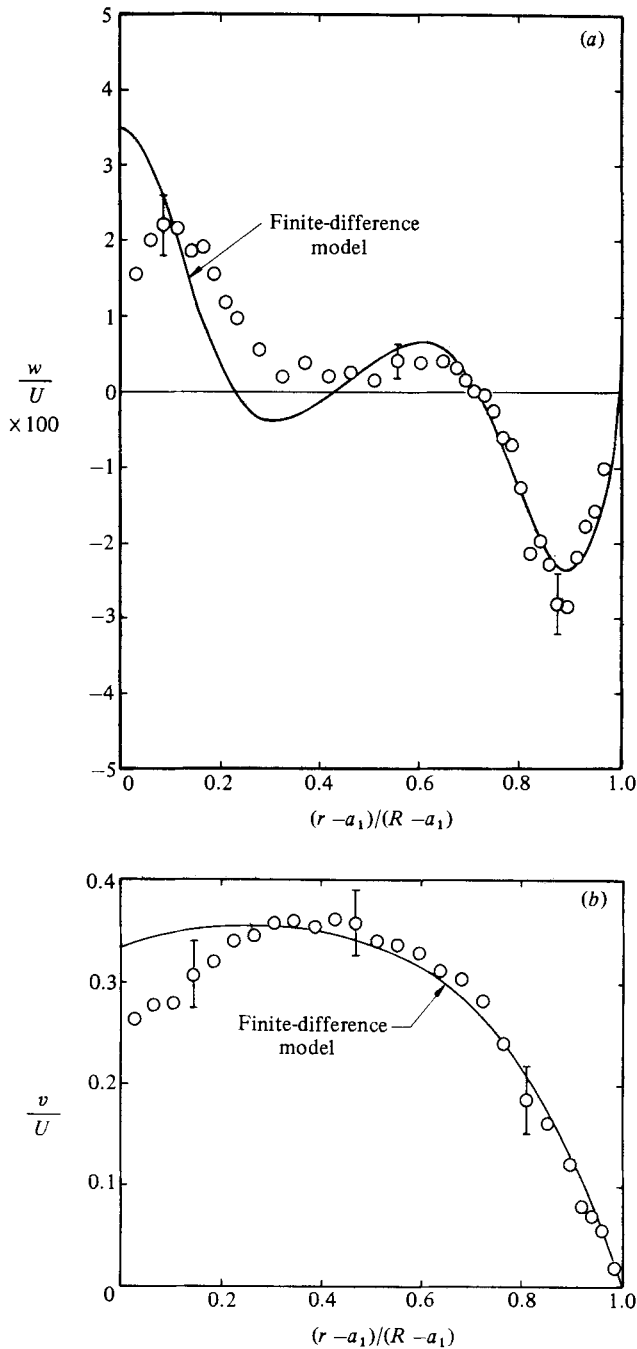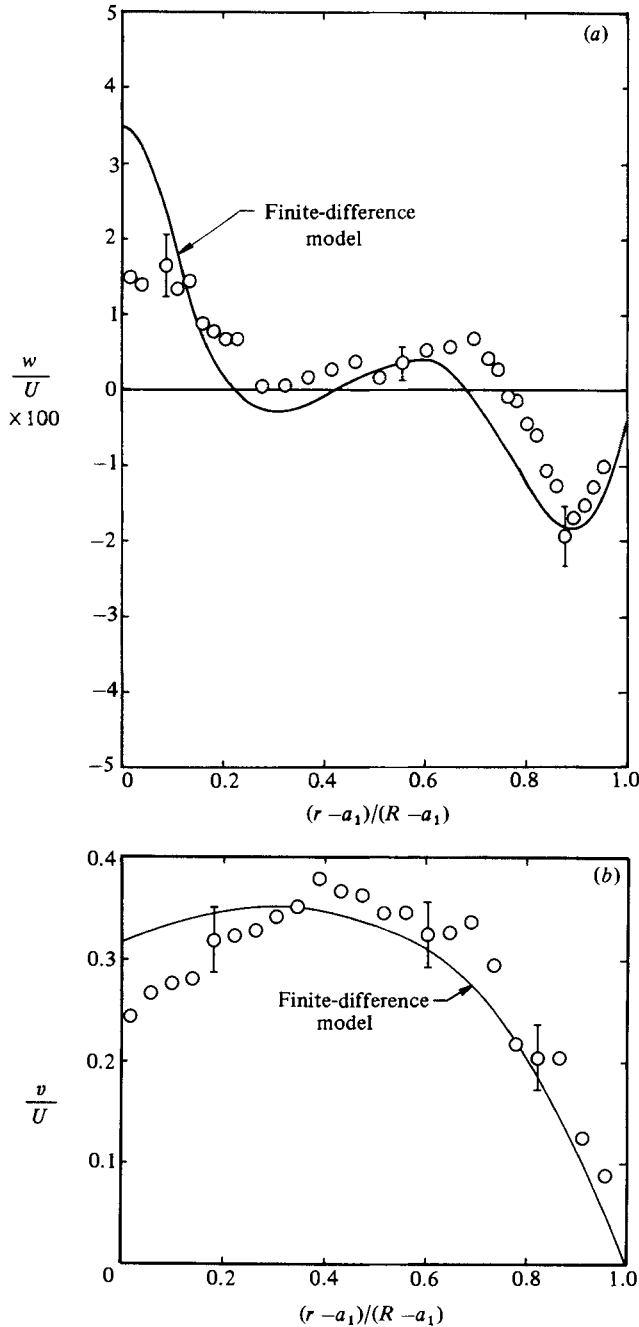
FIGURE 6. Radial distribution of the axial (a) and azimuthal (b) velocity at $z/L = 0.634$. Same parameters as in figure 5.

An LDV system measures fluid velocities at the intersection of two laser beams. The intersection of the two laser beams forms an ellipsoid that defines the boundaries of a volume in which measurements are made (Durst, Melling & Whitelaw 1976). In regions of steep velocity gradients, the result is an average velocity over the measuring volume. The spatial resolution in the radial direction of the LDV system

FIGURE 7. Radial distribution of the axial (a) and azimuthal (b) velocity at $z/L = 0.438$. Same parameters as in figure 5.

utilized in this experiment is 1.03 mm. This is 20 % of the thickness of the boundary layer along the free surface. Measurements taken when the measuring volume intersects the free surface would be low because the centroid of that portion of the measuring volume immersed in the fluid would be offset, in the direction away from the free surface, from the centroid of the whole measuring volume.

FIGURE 8. Radial distribution of the axial (*a*) and azimuthal (*b*)
velocity at $z/L = 0.242$. Same parameters as in figure 5.

The discrepancy between the experimental results and the numerical model may
also be partly due to the accuracy of the numerical model, which is influenced by
the grid spacing. Each Ekman layer is resolved only by about three grid spaces in
the axial direction. The axial circulation is driven by radial transport in the Ekman
layers, and a finer grid there would resolve the radial velocity profiles in the Ekman
layers better.
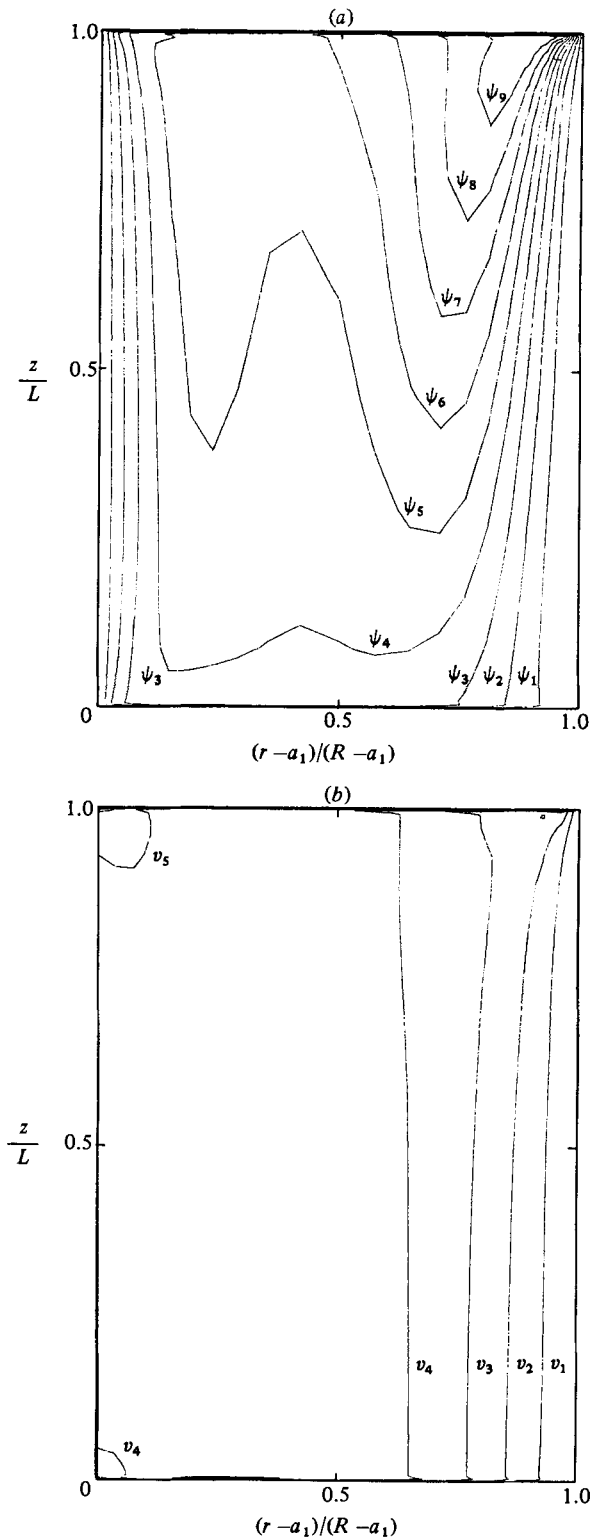
FIGURE 9. Streamlines (*a*) and contours of constant azimuthal velocity (*b*) calculated using the finite-difference simulation for the experimental conditions of figure 5. Streamline increment $= 0.61 \times 10^{-6}$ m^2/s, azimuthal-velocity contour increment $= 0.037$ m/s. Horizontal coordinate expanded by a factor of 7.3; the left edge is the free surface.
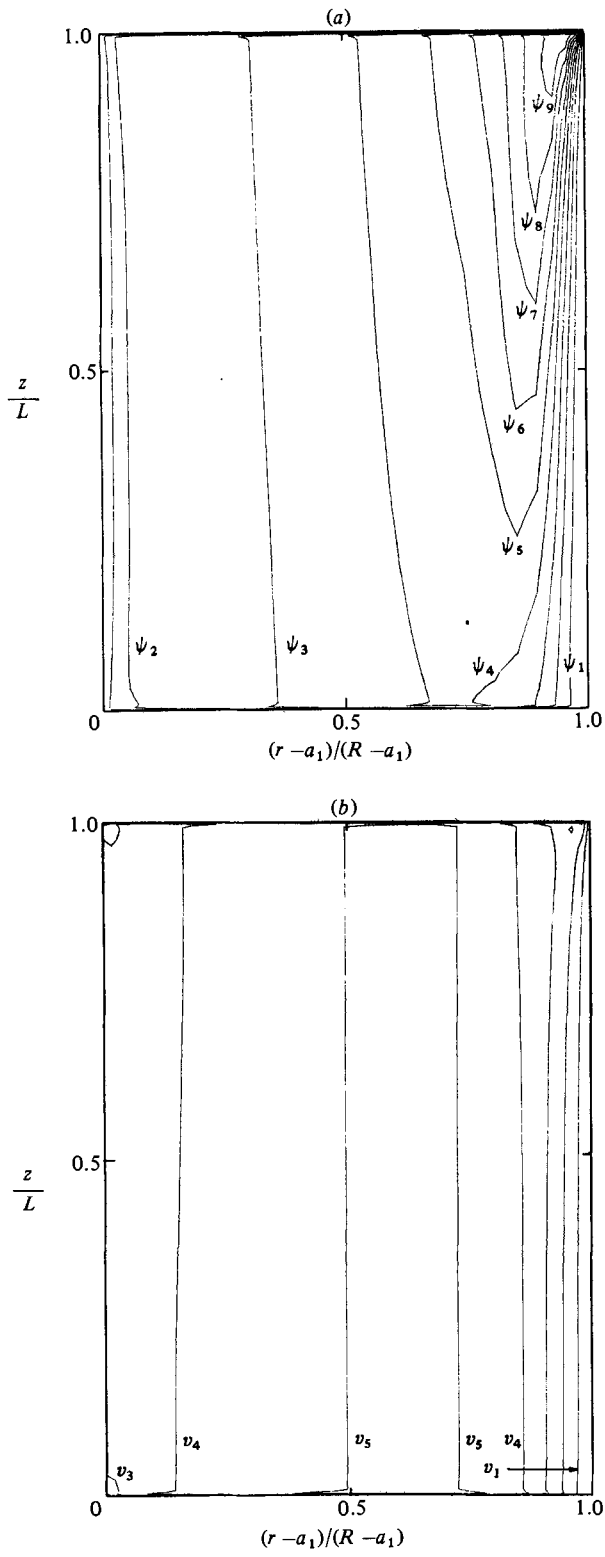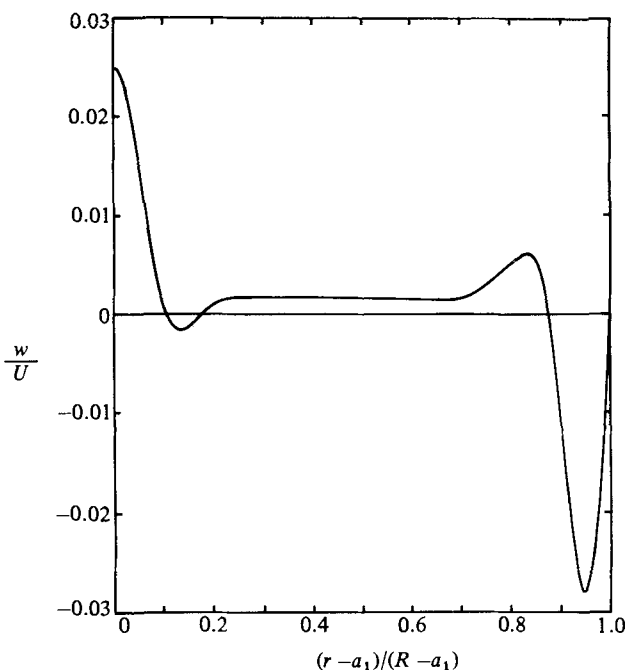
FIGURE 10. For caption see facing page.

FIGURE 11. Computed radial distribution of the axial velocity at midheight $(z/L = 0.5)$ for conditions of figure 10 (thick-film case).

Error bars for the experimental results show the magnitude of known random error in the measurements. The major source of random error in the azimuthal velocity measurements is the uncertainty in measuring the Doppler frequency on an oscilloscope. The principal sources of random error in the axial velocity measurements are the uncertainty of the azimuthal velocity measurements and the uncertainty in the measurements of the streamline slope angle θ. The latter uncertainty is due to the random error in the measurement of the $\pm 85°$ velocity components.

Figure 9 shows the streamlines and azimuthal velocity contours in the axial–radial plane, as predicted by the numerical model. The radial coordinate has been expanded so that details of the flow may be better seen. The axial circulation is driven by the Ekman layer on the disk at the top endcap of the rotor, and is primarily confined to boundary layers along the rotor wall and the free surface. Radial flow occurs in the Ekman layers at each endcap.

The thicknesses of boundary layers in rotating fluids are proportional to fractional powers of the Ekman number, a non-dimensional number analogous to the inverse Reynolds number in non-rotating flows:

$$E = \frac{\nu}{\Omega L^2}.$$

The horizontal Ekman layers are of thickness proportional to $E^{\frac{1}{2}}$. Two superimposed boundary layers form on the rotor sidewall. A thin layer, of thickness proportional

FIGURE 10. Streamlines (a) and contours of constant azimuthal velocity (b) calculated using the finite-difference model. Conditions same as in figure 5, but film thickness increased to 4.22 cm. Streamline increment $= 0.61 \times 10^{-6}$ m²/s; azimuthal-velocity contour increment $= 0.0365$ m/s. Horizontal coordinate expanded by a factor of 3.3.

to $E^{\frac{1}{3}}$, serves to transport fluid axially, and a thicker layer, proportional to $E^{\frac{1}{4}}$, accommodates the interior azimuthal velocity to the no-slip sidewall boundary condition. The single boundary layer along the free surface, transporting fluid axially, has a thickness proportional to $E^{\frac{1}{3}}$. Keeping in mind the expanded radial coordinate, the relative thicknesses of the sidewall and endwall boundary layers are readily evident in figure 9.

The flow investigated experimentally was a thin fluid film, dominated by thick boundary layers. In this case, there is no interior inviscid region. Another calculation was made in which all parameters other than the fluid film thickness were the same as in the flow investigated experimentally. The film thickness was increased from 1.905 cm to 4.22 cm. This new film thickness was chosen to ensure an interior region of inviscid flow. Streamlines and azimuthal velocity contours, for this case, are shown in figure 10. The axial velocity distribution in the fluid film at the rotor midplane is shown in figure 11. In addition to the weak axial flow in the interior, an axial boundary layer exists along the free surface.

Another calculation was run in which the nonlinear terms in the governing equations were deleted. The results were so similar to the calculated results presented in figures 5–9 that they are not presented here.

5. Discussion and conclusions

In a rotating cylinder completely filled with fluid, a sidewall $E^{\frac{1}{4}}$ boundary layer transports fluid axially between the top and bottom Ekman layers, and the return flow is spread over the entire interior region (Greenspan 1968). When the cylinder is partially filled and a free surface exists, radial transport in the Ekman layers remains the same as in the completely filled case. The mass flux that would have otherwise occurred in the empty interior then takes place along the free surface. This can be demonstrated by a linearized analysis of the Ekman layer attached to the top endcap.

The equations of motion, (2)–(5), can be linearized by assuming a small Rossby number ϵ. The steady-state equations are

$$\frac{1}{r}\frac{\partial}{\partial r}(ru) + \frac{\partial w}{\partial z} = 0, \tag{9}$$

$$-2v = -\frac{\partial P}{\partial r} + E\left(\nabla^2 u - \frac{u}{r^2}\right), \tag{10}$$

$$2u = E\left(\nabla^2 v - \frac{v}{r^2}\right), \tag{11}$$

$$0 = -\frac{\partial P}{\partial z} + E\nabla^2 w. \tag{12}$$

The above equations can be simplified for the Ekman layers by assuming that velocity gradients along the boundary layer, in the r-direction, are negligible in comparison with those across the boundary layers, in the z-direction. Using the interior flow conditions and the no-slip endcap as boundary conditions, the solution for the Ekman layer on the top endcap is (van Heijst 1979)

$$u_{\mathrm{E}} = \tfrac{1}{2}r\,\mathrm{e}^{-\zeta}\sin\zeta, \tag{13}$$

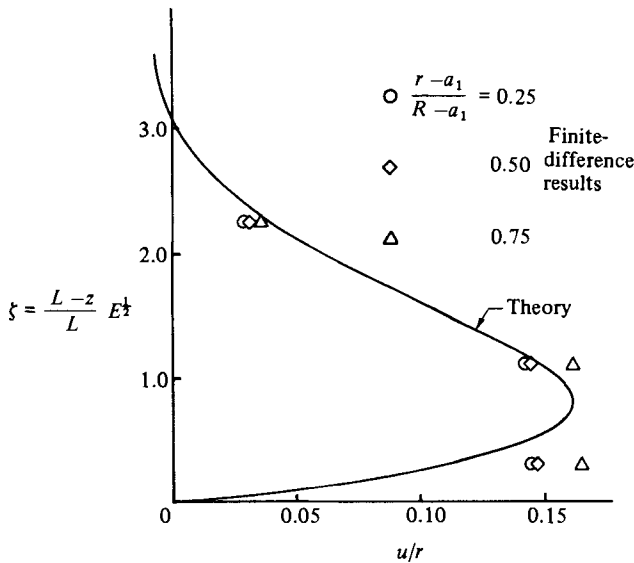$$v_{\mathrm{E}} = \tfrac{1}{2}r(1 + e^{-\zeta}\cos\zeta), \tag{14}$$

FIGURE 12. Computed radial-velocity profiles in the Ekman layer at
the top endcap for conditions of figure 10 (thick-film case).

with
$$\zeta = \frac{L-z}{L} E^{-\frac{1}{2}}, \tag{15}$$

where the dimensions of ζ are those shown in figure 1. Radial boundary conditions were not used in the evaluation of the Ekman-layer flow conditions, so this solution is equally applicable to filled and partially filled rotating cylinders. The radial velocity profile, computed using (13), is shown in figure 12 along with the finite-difference results at three radial positions for the thick-film case shown in figure 10. The invariant structure of the Ekman layer, with respect to the existence of a vertical free surface, is also demonstrated by the agreement between this linearized analysis and the plotted numerical results. The radial position $(r-a_1)/(R-a_1) = 0.75$ lies in the $E^{\frac{1}{4}}$ boundary layer along the rotor wall. The lower azimuthal velocity relative to inviscid flow accounts for the higher radial velocity in the top Ekman layer and the deviation of the numerical results, at this radial position, from those at the other two radial positions in figure 12. It follows for thin boundary layers that the ratio of axial mass flux in the boundary layer along the free surface to that attached to the rotor sidewall is proportional to the square of the ratio of the free surface radius to that of the sidewall:
$$\frac{\dot{m}_{a_1}}{\dot{m}_R} = \left(\frac{a_1}{R}\right)^2 \tag{16}$$

In conclusion, the effect of a vertical free surface on axial circulation in a rotating fluid is to concentrate the fluid, which in a completely filled container would have otherwise been recirculated in the fluid interior, into a thin shear layer along the free surface. All other aspects of the flow remain essentially unaltered from the case where the cylinder is completely filled with fluid. This conclusion agrees with a singular perturbation analysis by Greenspan (1982).

REFERENCES

BEARDSLEY, R. C., SAUNDERS, K. D., WARN-VARNAS, A. C. & HARDING, J. M. 1979 An experimental and numerical study of the secular spin-up of a thermally stratified rotating fluid. *J. Fluid Mech.* **93**, 161–184.

DURRANI, T. S. & GREATED, C. A. 1977 *Laser Systems in Flow Measurement.* Plenum.

DURST, F., MELLING, A. & WHITELAW, J. H. 1976 *Principles and Practice of Laser-Doppler Anemometry.* Academic.

GREENSPAN, H. P. 1968 *The Theory of Rotating Fluids.* Cambridge University Press.

GREENSPAN, H. P. 1982 Simulation of countercurrent flow in a gas centrifuge. *School of Engineering and Applied Sciences, University of Virginia, Report* UVA-ER-746-82U.

HEIJST, G. J. F. VAN 1979 Rotating flow in a cylinder with a circular barrier on the bottom. *J. Engng Maths* **31**, 153–171.

HIRT, C. W. 1979 Simplified solution algorithms for fluid flow problems. In *Numerical Methods for Partial Differential Equations* (ed. S. V. Parter), pp. 193–210. Academic.

RIBANDO, R. J. 1983 Incompressible flow in a rapidly rotating cylinder with a source/sink distribution in the lateral wall and a free inner boundary. *Int. J. Num. Meth. Fluids* (in press).

ROACHE, P. J. 1976 *Computational Fluid Dynamics.* Hermosa.

SHADDAY, M. A. 1982 Flow in a partially filled rotating cylinder. Ph.D. thesis, University of Virginia.

SWEET, R. A. 1973 Direct methods for the solution of Poisson's equation on a staggered grid. *J. Comp. Phys.* **12**, 422–428.